

Object-Based Arctic Sea Ice Ridge Detection From High-Spatial-Resolution Imagery

Xin Miao, Hongjie Xie, Stephen F. Ackley, and Songfeng Zheng

Abstract—High-spatial-resolution aerial photographs can provide detailed distribution of sea ice features. However, very few studies have ever considered shadows on the photographs for sea ice detection. In this letter, sea ice shadows, retrieved from 163 selected aerial photographs acquired on July 26, 2010, in a marginal-ice-zone area near Barrow, Alaska, utilizing an object-based classification scheme, are used to estimate the sea ice ridge attributes through local solar illumination geometry. The photograph-averaged ridge frequency ($354.6\text{--}8908.7\text{ km}^{-2}$), length (1.22–10.33 m), and height (0.15–1.29 m) are obtained from the 163 photographs using batch processing. This letter provides an important batch processing method for ridge detection and ridge attribute retrieval from the high-resolution imagery of sea ice.

Index Terms—Aerial photography, pressure ridge, shadow, sea ice.

I. INTRODUCTION

THE arctic sea ice acts as an indicator and an amplifier of climate change. Most studies, however, focus primarily on the spatial distribution of sea ice 2-D features, such as ice/snow, water, and melt ponds derived from moderate or very high spatial resolution (VHR) optical images [1]–[3]. Seldom do studies consider *pressure ridges* from VHR aerial photographs. A pressure ridge usually develops in a sea ice cover as a result of a stress regime driven by currents and winds [4], [5]. Ridges are the thickest sea ice features and account for about one-half of the total sea ice volume [6]–[8]. As an important sea ice mechanical and mass distribution feature, attributes of pressure ridges can be used to refine, validate, and improve sea ice and climate models. Although numerous studies have demonstrated that pressure ridges can be extracted from synthetic aperture radar (SAR) signatures or airborne LiDAR profiles [9], [10], the data are relatively scarce. In addition, spatial resolution is usually limited for SAR data. On the other hand, a large collection

of VHR aerial photographs has become available in Arctic and Antarctic regions in recent years, including IceBridge airborne data [11] and many helicopter-based aerial photographs during polar expeditions.

In this letter, we extend our previous research and develop an efficient batch processing algorithm that can automatically detect the location and profile of pressure ridges using VHR aerial photographs based on shadow geometry. Two related works include the detection of sea ice deformation features using a single GeoEye-1 image [12], and ridge height measurements using declassified satellite images of Arctic sea ice [13]. These shadow detection methods were either manual or semimanual for a limited number of images. In our previous work, we developed a scheme of object-based sea ice, melt pond, and shadow classification from aerial photographs [14]. This letter aims to accomplish the following: 1) to extract reliable sea ice ridge attributes such as normalized ridge density, average ridge length, and average ridge height through local solar illumination geometry and 2) to provide quantitative uncertainty analysis for derived ridge attributes. The method would be efficient enough for batch image processing and adapt well to different light conditions.

II. STUDY AREA AND AERIAL IMAGE PREPROCESSING

The aerial photographs used in this letter were obtained on July 26 during the Fourth Chinese National Arctic Research Expedition in 2010 (CHINARE 2010). The expedition was conducted with the Chinese Research Vessel Xuelong from July 21 to August 28, 2010 [15]. The flight on July 26 was in the marginal ice zone (MIZ) at around 72°N near Barrow, Alaska. The aerial photographs were taken by a Canon G9 camera [3]. The focal length was set as 7.4 mm, with the field of view of $205.4\text{ m} \times 154.1\text{ m}$ at the typical flight height of 200 m. The resampled photograph resolution was 1000×750 pixels. The associated independently measured GPS positions and altitude were geotagged to the aerial photographs. More details of this flight mission can be found in [14] and [15].

III. METHODS

A. Shadow Detection

Shadow and three nonshadow sea ice classes, i.e., water, ice/snow, and general submerged ice (GSI), can be visually identified from VHR aerial photographs (see Table I). All four general sea ice types have rather homogeneous texture within each class and generally show distinct between-class

Manuscript received September 11, 2015; revised January 23, 2016 and February 21, 2016; accepted March 19, 2016. Date of publication April 11, 2016; date of current version May 19, 2016. The work of S.F. Ackley was supported by the Office of Naval Research under Grant N000141310435.

X. Miao is with the Department of Geography, Geology and Planning, Missouri State University, Springfield, MO 65897 USA, and also with the Laboratory for Remote Sensing and Geoinformatics and Department of Geological Sciences, University of Texas at San Antonio, San Antonio, TX 78249 USA (e-mail: XinMiao@missouristate.edu).

H. Xie and S. F. Ackley are with the Laboratory for Remote Sensing and Geoinformatics and Department of Geological Sciences, University of Texas at San Antonio, San Antonio, TX 78249 USA.

S. Zheng is with the Department of Mathematics, Missouri State University, Springfield, MO 65897 USA.

Color versions of one or more of the figures in this paper are available online at <http://ieeexplore.ieee.org>.

Digital Object Identifier 10.1109/LGRS.2016.2544861

TABLE I
OBJECT-BASED CLASSIFICATION SCHEME FOR DETECTION
OF SEA ICE FEATURES FROM AERIAL PHOTOGRAPHS

Class Name		Class Description
Shadow		Darker objects on the ice/snow caused by ridges and low solar elevation angle.
Non-shadow	Water	Arctic ocean, objects are rather dark and smooth.
	General submerged ice (GSI)	Ice submerged under water along floe edges and melt ponds.
	Ice/snow	Bright white objects due to high reflectance of ice/snow.

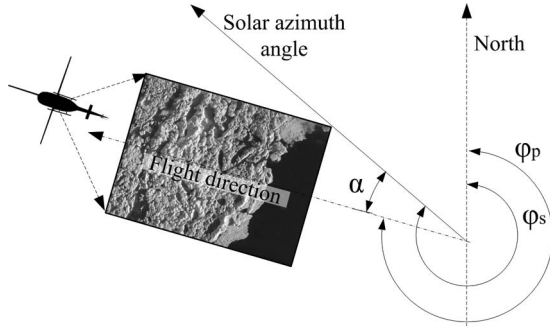


Fig. 1. Photograph-based solar radiation azimuth (α) can be calculated from the solar azimuth (φ_s) and flight direction (φ_p).

boundaries. Therefore, we adopt an object-based classification approach to identify shadows [14]. After image segmentation, a total of 13 spectral, texture, and spatial attributes are imported into the *random forest* classifier to detect shadows. Interested readers are referred to [14] for details about the method.

B. Ridge Detection

The extracted shadow polygons are imported to the ArcPython to estimate sea ice ridges or roughness based on solar illumination geometry. The solar azimuth angle and elevation angle are retrieved from PyEphem, which provides astronomical computations given a time and a location. The photograph rotation angles (α) are calculated from the flight direction and the camera installation geometry on the aircraft

$$\alpha = \varphi_s - \varphi_p + c \quad (1)$$

where α is the photograph-based solar radiation azimuth, φ_s is the solar azimuth, φ_p is the flight direction, $c = 0$ when $\alpha > 0$, and $c = 360$ when $\alpha < 0$ (see Fig. 1).

In order to estimate ridge attributes, the shadow polygon should be rotated by $(90-\alpha)$ and then rasterized using a predefined cell size. The shadow length is then estimated by counting the cells of each shadow object along the x -axis as shown in Fig. 2, and converted to physical measurements based on the cell size. By this way, a shadow profile, including shadow length and width, can be extracted. The ridge length is equivalent to the shadow length, while the ridge height (R_H) can be derived from the shadow width (S_w)

$$R_H = S_w \cdot \tan(\beta_e) \quad (2)$$

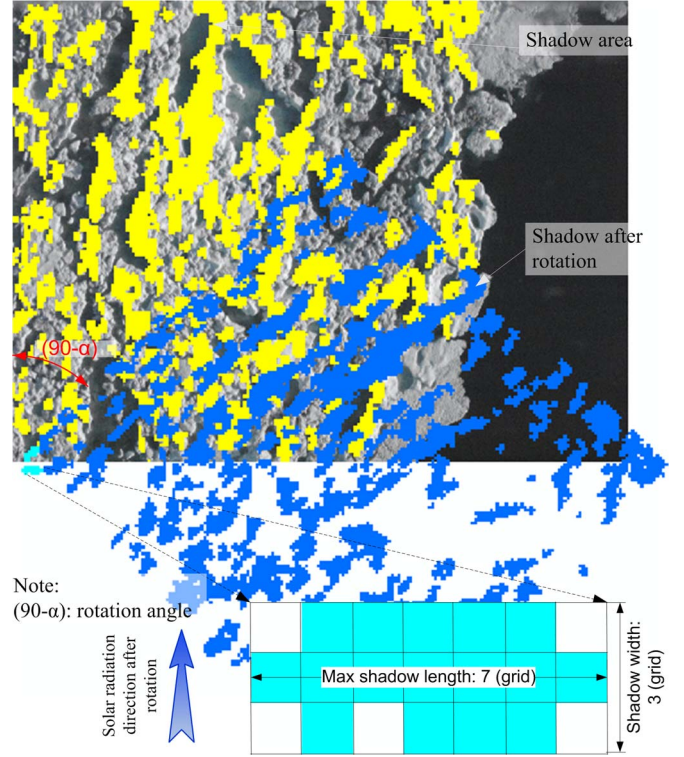


Fig. 2. Shadow profile can be derived by photograph rotation, rasterization, and cell counting.

where β_e is the solar elevation angle. The average height for each ridge ($\overline{R_H}$) is the mean of the R_H along the ridge profile/length

$$\overline{R_H} = \frac{\sum R_H}{n} \quad (3)$$

where n is the number of cells along the shadow/ridge length.

C. Uncertainty Analysis

Aside from the shadow classification error, there are two major error sources when determining ridge positions and heights. First, since the shadow length and width are used to derive ridge attributes, we conduct a quantitative scale uncertainty analysis based on the helicopter attitude and flight height. In a low relief variation situation such as sea ice detection, the scale is mainly affected by the magnitude and angular orientation of the photograph tilt [16]. Considering a tilted photograph without rotation, the scale factor can be estimated as

$$S_t = \left(\frac{f / \cos t - (f \tan \beta + f \tan t) \sin t}{H} \right) \cdot \cos(t)^{-1/2} \\ = \left[(\sec t)^{\frac{1}{2}} \cdot (\sec t - (\tan \beta + \tan t) \cdot \sin t) \right] \cdot S_v \quad (4)$$

where S_t is the tilted photograph scale, S_v is the corresponding vertical photograph area scale, t is the tilt angle, and β is the direction angle of a pixel relative to the optical axis in the principle plane. Considering the extreme situation, β is the half of the maximum field of view angle of 27.2° (positive when toward the tilt direction and negative when against the tilt

direction), and the maximum value of t is 6° for the helicopter; then, the sizes of pixels on the tilted photograph represent 0.95–1.06 times that on the vertical photograph. Therefore, the upper limit of the relative linear uncertainty due to helicopter attitude σ_a is 6%. Second, the photograph scale change (dS) with GPS measurement error of flight height is

$$dS = -\frac{f}{H^2} \cdot dH = -\frac{dH}{H} \cdot S \quad (5)$$

where $S = f/H$ is the scale for the vertical photograph. Supposing that the typical H is 200 m and the GPS measurement error dH is 5 m, then the relative uncertainty of the linear feature due to the flight height changes σ_h is 2.5%. Another possible error source is the solar elevation angle. Since the photograph time was geotagged through GPS and the error is less than 3 s, the corresponding error of the solar elevation angle is less than 0.005° based on astronomical computation. As a result, the ridge height should only have an error of less than 0.001 m which can be neglected.

IV. RESULTS AND DISCUSSION

A. Shadow Classification

Shadows are extracted from all 163 aerial photographs through the object-based random forest classifier. The accuracy of shadow extractions is assessed through a total of 178 ground reference samples of four general classes (see Table I) that have various light conditions. Shadow shows a high user's accuracy of 88.9% and producer's accuracy of 91.4% [14]. The classification uncertainty

$$\sigma_c = \sqrt{\sigma_I(1 - \sigma_I)/n + \sigma_{II}(1 - \sigma_{II})/n} \quad (6)$$

where the producer's error σ_I (measure of omission) is 0.09, the user's error σ_{II} (measure of commission) is 0.11, and $n = 178$ is the number of test samples. Therefore, the upper limit of σ_c for the total number of shadow objects is 0.03 or 3%.

The major source of error in shadow detection is the spectral variability. Shadow samples are selected only in sea ice regions in this letter, so a shadow object with a mixture of water, melt ponds, or ice/snow becomes elusive. Four aerial photographs in different sea ice retreating stages (a1–d1), their classification results (a2–d2), and the corresponding reference maps (a3–d3) acquired through extensive visual inspection are illustrated in Fig. 3, and seven typical shadow detection errors (e1–e7) are labeled. Most of them are caused by the complex mixture of shadow and nonshadow classes. For example, e1, e2, e4, e5, and e6 are caused because the shadow on melt ponds or ice is mistakenly classified as GSI, and e3 is a missed melt pond hidden in the shadow. In an extreme case, wet ice/snow can even be wrongly classified as shadow (e7).

B. Ridge Attributes and Uncertainty Analysis

Each rasterized shadow object is used to derive the corresponding ridge length and average ridge height. Then, three ridge statistics are derived for each photograph as follows.

1) Normalized sea ice ridge density (D_p)

$$D_p = \frac{N_r}{A_p(1 - r_w)} \quad (7)$$

where N_r is the total number of ridges in the current photograph, A_p is the total coverage area of the photograph, and r_w is the percentage of water within this photograph. The spatial distribution and histogram of normalized ridge densities for 163 photographs are illustrated in Fig. 4(a). The average ridge density across these photographs is $2384.0 \pm 5.6 \text{ km}^{-2}$.

2) Sea ice ridge length (R_{pl})

$$R_{pl} = \frac{\sum_{N_r} R_l}{N_r} \quad (8)$$

where R_l is the length of each ridge in a photograph. The spatial distribution and histogram of photograph average ridge lengths for 163 photographs are illustrated in Fig. 4(b). The propagated relative uncertainty is $\sigma_{pl} = \sqrt{(\sigma_a^2 + \sigma_h^2)/N_r}$, so the estimated uncertainty of the photograph average ridge length ranges from 0.003 to 0.025 m.

3) Sea ice ridge height (R_{ph})

$$R_{ph} = \frac{\sum_{N_r} \overline{R_H}}{N_r} \quad (9)$$

where $\overline{R_H}$ is the average height for each ridge in the photograph. The spatial distribution and histogram of photograph average ridge heights for 163 photographs are illustrated in Fig. 4(c). The propagated relative uncertainty is $\sigma_{ph} = \sqrt{(\sigma_a^2 + \sigma_h^2)/N_r} \cdot \tan(\beta_e)$, so the estimated uncertainty of photograph average ridge heights ranges from 0.0004 to 0.005 m.

Each dot in Fig. 4 represents an aerial photograph, and it can be regarded as a sample for the continuous sea ice continuum. The normalized ridge density is from 354.6 to 8908.7 km^{-2} , while most of the photographs have a density between 1000 and 2000 km^{-2} [see Fig. 4(a)]. It means that most of the sea ice in MIZ has a rough surface, and at least one ridge can be found per $30 \times 30 \text{ m}^2$ on the average. The photograph average ridge length is 1.22–10.33 m, while most of the photographs have an average ridge length of 2–5 m [see Fig. 4(b)]. The photograph average ridge height is from 0.15 to 1.29 m, while most of the photographs have an average ridge height of 0.9–1.1 m [see Fig. 4(c)]. By correlating the subimages in Fig. 4, it is clear that areas with high ridge density usually have short ridge length and low height, and the inverse is also true (i.e., low ridge density has longer ridge length and higher height).

It is worth noting that the proposed method has three potential error sources. First, the actual position of a ridge is radially shifted from the principle point due to relief displacement d

$$d = \frac{r \cdot h}{H} \quad (10)$$

where r is the radial distance, h is the height of the ridge, and H is the flight height. Supposing that H is around 200 m, h is less than 2 m, and the maximum value of r is 625 pixels (on four

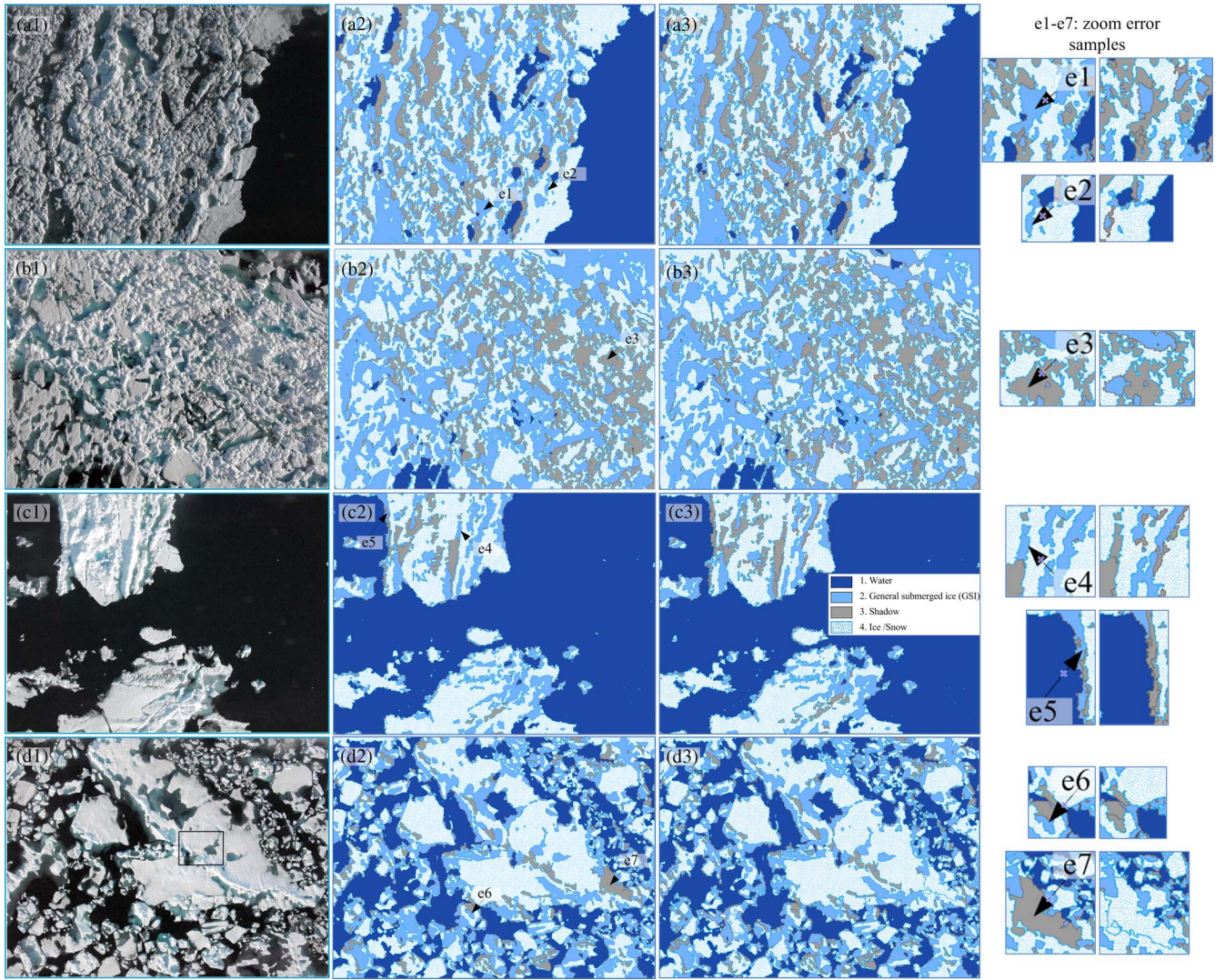


Fig. 3. Illustration of aerial photographs (a1–d1), shadow /nonshadow classification results (a2–d2), and reference maps (a3–d3). Examples of shadow errors are labeled as e1–e7.

corners of a photograph), then the upper limit of d is 6.25 pixels or 1.25 m. Therefore, the geolocation error of the ridges is less than 1.25 m due to the radial relief displacement. Nevertheless, this geolocation error will not significantly affect the estimation of ridge length or height since shadow on the flat ground has no much relief displacement. Second, if the sea ice surface is not smooth and flat and has a gentle slope, the ridge height could have a positive or negative bias, depending on the actual position of the ridges. Third, when two series of parallel ridges are close enough, their shadows can be overlaid so that ridge heights can be overestimated. Since a photograph ridge height is the average value of all ridges within the photograph coverage and the total number of ridges for each photograph ranges from 34 to 429 with a mean of 188 for the 163 photographs, the statistical errors from the latter two sources are not significant.

Interesting enough, the statistics of ridge density and ridge length derived from aerial photographs are not totally compatible with the field records of CHINARE 2010, where the observed ridge density is much lower (around 300 km^{-2}) and the average ridge length is at least 20 m. We believe

that it is because multiple shadow objects along a certain direction could belong to one long ridge. This is evidenced in that the derived average ridge length is only 2–5 m and multiple ridge shadows are aligned well as seen in Fig. 3 and a better understanding of. However, the estimated statistics provide a detailed surface roughness estimation and a better understanding of fragmented ridge distribution. Furthermore, our photograph-averaged ridge height (0.15–1.29 m) is generally compatible with the CHINARE 2010 observation but smaller than the average sail height in the Beaufort Sea of 1.6 m [4]. We believe our result most likely reflects the localized sea ice ridge variation in the hot summer (end of July) at the highly segmented MIZ area.

V. CONCLUSION

We developed an effective and efficient object-based Arctic sea ice shadow detection and ridge estimation algorithm for high-spatial-resolution aerial photographs based on local solar illumination geometry. Three ridge statistics and their

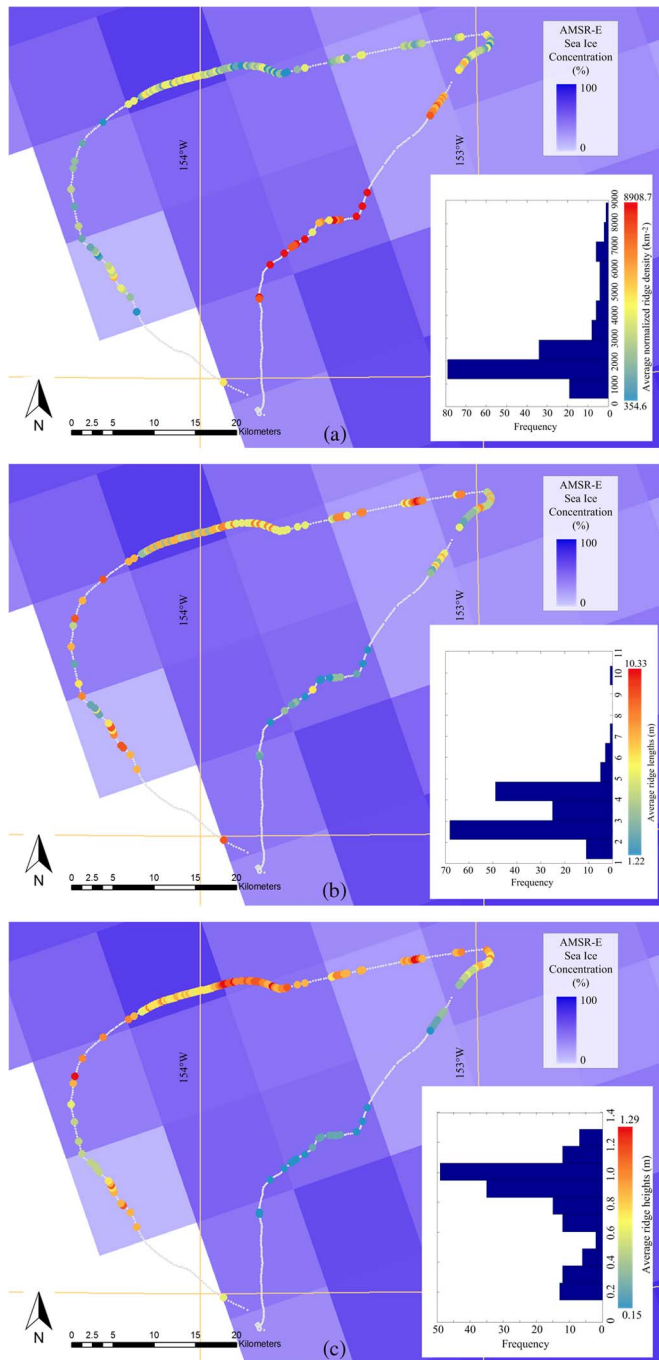


Fig. 4. Spatial distribution and histogram of (a) photograph normalized sea ice ridge density, (b) photograph average sea ice ridge lengths, and (c) photograph average sea ice ridge heights. The colored dots represent 163 aerial photographs with different average ridge heights. The background is the AMSR-E sea ice concentration map (the same day) with the spatial resolution of 12.5 km.

uncertainties are derived from each photograph: normalized sea ice ridge density (D_p), photograph-averaged sea ice ridge length (R_{pl}), and photograph-averaged sea ice ridge height (R_{ph}). Future work includes the following: 1) combining small

fragmented ridges into a complete winding ridge; 2) scaling up the ridge attributes to validate sea ice models; and 3) sea ice surface reconstruction and LiDAR validation.

ACKNOWLEDGMENT

Author H. Xie would like to thank the Chinese Arctic and Antarctic Administration for the opportunity to participate in the 2010 Chinese Arctic Expedition. The authors would like to thank R. Lei, W. Huang, C. Ke, and many others for collecting those aerial photographs.

REFERENCES

- [1] A. H. H. Renner, M. Dumont, J. Beckers, S. Gerland, and C. Haas, "Improved characterisation of sea ice using simultaneous aerial photography and sea ice thickness measurements," *Cold Regions Sci. Technol.*, vol. 92, pp. 37–47, Aug. 2013.
- [2] V. D. Onana *et al.*, "A sea-ice lead detection algorithm for use with high-resolution airborne visible imagery," *IEEE Trans. Geosci. Remote Sens.*, vol. 51, no. 1, pp. 38–56, Jan. 2013.
- [3] P. Lu, Z. J. Li, B. Cheng, R. B. Lei, and R. Zhang, "Sea ice surface features in Arctic summer 2008: Aerial observations," *Remote Sens. Environ.*, vol. 114, no. 4, pp. 693–699, Apr. 2010.
- [4] L. Strub-Klein and D. Sudom, "A comprehensive analysis of the morphology of first-year sea ice ridges," *Cold Regions Sci. Technol.*, vol. 82, pp. 94–109, Oct. 2012.
- [5] W. D. I. Hibler and S. F. Ackley, "Height variation along sea ice pressure ridges and the probability of finding 'holes' for vehicle crossings," *J. Terramech.*, vol. 12, pp. 191–199, 1975.
- [6] M. Leppäranta, *The Drift of Sea Ice*. New York, NY, USA: Springer-Verlag, 2005.
- [7] E. C. Hunke and W. H. Lipscomb, CICE: The Los Alamos Sea Ice Model—Documentation and Software User's Manual, Version 4.0, T-3 Fluid Dyn. Group, Los Alamos Nat. Lab., Los Alamos, NM, USA, 2010.
- [8] C. Haas, Q. Liu, and T. Martin, "Retrieval of Antarctic sea-ice pressure ridge frequencies from ERS SAR imagery by means of *in situ* laser profiling and usage of a neural network," *Int. J. Remote Sens.*, vol. 20, no. 15/16, pp. 3111–3123, Oct. 15 1999.
- [9] M. Gupta, D. G. Barber, R. K. Scharien, and D. Isleifson, "Detection and classification of surface roughness in an Arctic marginal sea ice zone," *Hydrol. Process.*, vol. 28, no. 3, pp. 599–609, Jan. 2014.
- [10] H. Melling, "Detection of features in first-year pack ice by synthetic aperture radar (SAR)," *Int. J. Remote Sens.*, vol. 19, no. 6, pp. 1223–1249, Apr. 1998.
- [11] X. Wang, H. Xie, Y. Ke, S. F. Ackley, and L. Liu, "A method to automatically determine sea level for referencing snow freeboards and computing sea ice thicknesses from NASA IceBridge airborne LiDAR," *Remote Sens. Environ.*, vol. 131, pp. 160–172, Apr. 15, 2013.
- [12] I. Zakharov, P. Bobby, D. Power, S. Warren, and M. Howell, "Detection and characterization of extreme ice features in single high resolution satellite imagery," in *Proc. IEEE Int. Geosci. Remote Sens. Symp.*, 2014, pp. 3965–3968.
- [13] R. Kwok, "Declassified high-resolution visible imagery for Arctic sea ice investigations: An overview," *Remote Sens. Environ.*, vol. 142, pp. 44–56, Feb. 2014.
- [14] X. Miao, H. Xie, S. F. Ackley, D. K. Perovich, and C. Ke, "Object-based detection of Arctic sea ice and melt ponds using high spatial resolution aerial photographs," *Cold Regions Sci. Technol.*, vol. 119, pp. 211–222, 2015.
- [15] H. Xie *et al.*, "Summer sea ice characteristics and morphology in the Pacific sector as observed during the CHINARE 2010 cruise," *Cryosphere*, vol. 7, pp. 1057–1072, 2013.
- [16] P. R. Wolf and B. A. Dewitt, *Elements of Photogrammetry: With Applications in GIS*, 3rd ed. Boston, MA, USA: McGraw-Hill, 2000.